

## Creep behavior in interlaminar shear of a Hi-Nicalon™/SiC-B<sub>4</sub>C composite at 1200°C in air and in steam

Marina Ruggles-Wrenn<sup>a</sup> and Matthew Pope

Air Force Institute of Technology, Wright-Patterson Air Force Base, Ohio 45433-7765, USA

**Abstract.** Creep behavior in interlaminar shear of a non-oxide ceramic composite with a multilayered matrix was investigated at 1200°C in laboratory air and in steam environment. The composite was produced via chemical vapor infiltration (CVI). The composite had an oxidation inhibited matrix, which consisted of alternating layers of silicon carbide and boron carbide and was reinforced with laminated Hi-Nicalon™ fibers woven in a five-harness-satin weave. Fiber preforms had pyrolytic carbon fiber coating with boron carbon overlay applied. The interlaminar shear properties were measured. The creep behavior was examined for interlaminar shear stresses in the 16–22 MPa range. Primary and secondary creep regimes were observed in all tests conducted in air and in steam. In air and in steam, creep run-out defined as 100 h at creep stress was achieved at 16 MPa. Similar creep strains were accumulated in air and in steam. Furthermore, creep strain rates and creep lifetimes were only moderately affected by the presence of steam. The retained properties of all specimens that achieved run-out were characterized. Composite microstructure, as well as damage and failure mechanisms were investigated. The tested specimens were also examined using electron probe microanalysis (EPMA) with wavelength dispersive spectroscopy (WDS). Analysis of the fracture surfaces revealed significant surface oxidation, but only trace amounts of boron and carbon. Cross sectional analysis showed increasing boron concentration in the specimen interior.

### 1. Introduction

Advanced aerospace applications such as turbine engine components, hypersonic missiles and flight vehicles, and spacecraft reentry thermal protection systems require structural materials that have superior long-term mechanical properties and retained properties under high temperature, high pressure, and varying environmental factors. Ceramic-matrix composites (CMCs) are prime candidates for such applications.

Because of their low density, high strength and fracture toughness at high temperatures SiC fiber-reinforced SiC matrix composites are currently being evaluated for aircraft engine hot-section components [1–4]. Since their constituents are intrinsically oxidation-prone, oxidation embrittlement is the most significant problem hindering SiC/SiC composites [5]. Typically the embrittlement occurs once oxygen enters through the matrix cracks and reacts with the fibers and the fiber coatings [6–8]. The degradation of fibers and fiber coatings is generally accelerated in the presence of moisture [9].

---

<sup>a</sup>Corresponding author: [marina.ruggles-wrenn@afit.edu](mailto:marina.ruggles-wrenn@afit.edu)

The issue of improving the oxidation resistance of the SiC/SiC composites has been addressed through the design of innovative multilayered interphases [10–12] and of self-healing multilayered matrices [10, 12–16]. The multilayered matrices contain phases that facilitate glass formation at high temperature thus healing the cracks and preventing oxygen from diffusing further into the composite and reaching the oxidation-prone fibers.

Numerous recent studies investigated mechanical behavior of high-performance SiC/SiC composites at elevated temperature [17–27]. Efforts to assess the life-limiting behaviors of SiC/SiC CMCs have been focused mainly on the fiber-dominated properties. However, due to the inherent material defects in the matrix-rich or fiber-matrix interface regions, fiber-reinforced woven CMCs are often susceptible to failure under interlaminar tensile or shear stress. The interlaminar failure or delamination may cause the loss of stiffness and accelerate structural failure of the CMC component [28, 29]. Therefore a thorough understanding of the performance of SiC/SiC composites under interlaminar stresses in service environments is critical to design and life prediction for these materials.

Several authors have examined the high-temperature behavior in interlaminar shear of various 2D woven CMCs. Choi et al. [28–32] evaluated high-temperature behavior in interlaminar shear of SiC/BSAS, SiC/MAS, C/SiC, and Hi-Nicalon™/SiC composites using double notch shear (DNS) specimens. Interlaminar shear strength (ILSS) values of 30–50 MPa were reported. Choi and co-workers established the ILSS as a function of loading rate and demonstrated that the ILSS degraded with decreasing loading rate. It was concluded that the life of these CMCs in shear was limited by slow crack growth (SCG) or damage accumulation. A phenomenological, power-law crack growth model was proposed to account for the degradation of ILSS. Model predictions were in good agreement with experimental results. All experimental data reported by Choi and co-workers were obtained at elevated temperature in air. Recently Ruggles-Wrenn and Laffey [33] studied creep behavior in interlaminar shear of an oxide/oxide composite (Nextel™720/alumina) CMC at 1200°C in air and in steam. The creep lifetimes were drastically reduced in the presence of steam.

This study investigates the creep behavior in interlaminar shear of a CVI ceramic composite comprised of Hi-Nicalon™ fibers, pyrolytic carbon fiber coating with boron carbide overlay and a SiC-based multilayered matrix. The oxidation inhibited matrix consists of alternating layers of SiC and B<sub>4</sub>C. Interlaminar shear creep tests were conducted at 1200°C in air and in steam environments. The composite microstructure as well as damage and failure mechanisms were examined. To better understand the post-test atomic composition of the composite material, electron probe microanalysis (EPMA) with wavelength dispersive spectroscopy (WDS) was performed.

## 2. Material and experimental arrangements

The test material was Hi-Nicalon™/SiC-B<sub>4</sub>C (Hi-N/SiC-B<sub>4</sub>C) ceramic composite fabricated by Hyper-Therm High-Temperature Composites, Inc. (Huntington Beach, CA). The CMC was reinforced with Hi-Nicalon™ fibers woven in a five-harness satin weave, and was processed by CVI. The matrix consists of alternating layers of silicon carbide and boron carbide. Laminated fiber preforms were produced from 18 plies of woven fabric in a 0/90 layup symmetric about mid-plane with warp and fill plies alternated. Prior to infiltration, the preforms were coated with pyrolytic carbon fiber coating (~0.40 μm thick) with boron carbide overlay (~1.0 μm thick) to decrease bonding between fibers and matrix. The composite had a finished fiber volume of ~36.4% and a density of ~2.40 g/cm<sup>3</sup>. The overall microstructure of the CMC is presented in Fig. 1.

All tests were performed at 1200°C using the experimental set-up detailed elsewhere [25]. In all tests, a specimen was heated to test temperature at 1°C/s, and held at temperature for additional 30 min prior to testing. The same procedures were used for testing in air and in steam. The double-notch shear (DNS) specimens measuring 150 mm × 20 mm × 5 mm were used in all tests. The notches of 0.5-mm width were extended to the mid-plane of each test specimen so that shear failure occurred on the plane

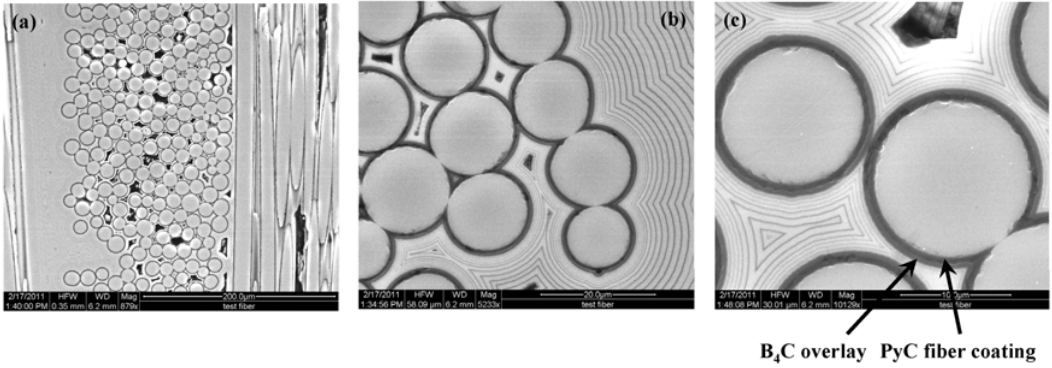


**Figure 1.** (a) Typical composite microstructure. (b) Self-healing matrix consisting of alternating layers of SiC and B<sub>4</sub>C. (c) Fibers and PyC fiber coating with B<sub>4</sub>C overlay.

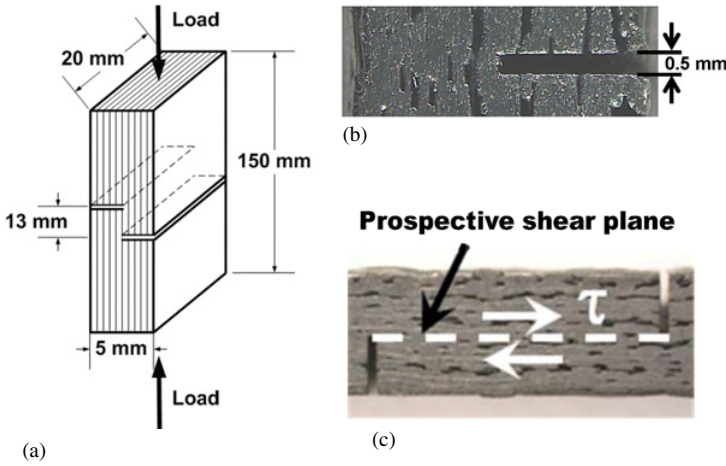


**Figure 2.** (a) Double-notch shear specimen. (b) Notch details. (c) Prospective shear plane.

between the notch tips. The test specimens were sealed with a CVI SiC overcoat after machining. The distance between the notches was 13 mm. Schematic of the DNS specimen and notch details are shown in Figs. 2a and 2b, respectively. The 13-mm distance between the notches permits the measurement of compressive strain between the notch tips with an MTS high-temperature extensometer of 12.5-mm gage length (see Ruggles-Wrenn et al. [25] for extensometer information). For strain measurement, the extensometer rods were placed as close to the notch tips of the specimen as possible. All DNS specimens were loaded in compression along the specimen axis (Fig. 2a) to produce failure by interlaminar shear along the shear plane between the notches (Fig. 2c). Compression tests to failure were performed with the constant stress rate of 12 MPa/s. The same stress rate was used to load specimens to the creep stress level in creep-rupture tests. Creep run-out was defined as 100 h at a given creep stress. All specimens that achieved creep run-out were tested in compression to failure at 1200°C in air to evaluate the retained interlaminar properties.

The shear stress,  $\tau$ , between the notches along the shear plane was calculated in accordance with the ASTM Standard C1425 [34] as:

$$\tau = \frac{P}{Wh} \cdot \quad (1)$$

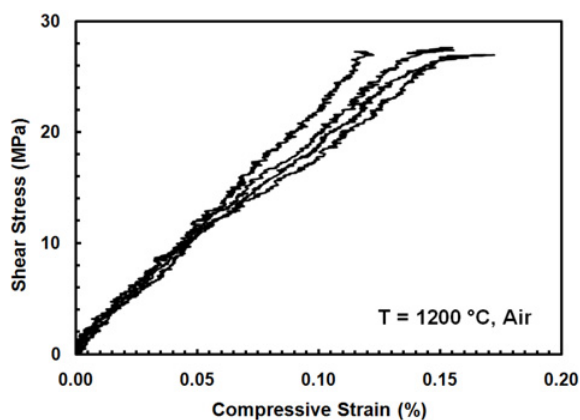


**Figure 3.** Interlaminar shear stress vs. compressive strain curves for Hi-N/SiC-B<sub>4</sub>C at 1200°C in air.

Here  $P$  is the applied force,  $W$  is the specimen width, and  $h$  is the distance between the notches. While the shear stress distribution between the notches is not uniform, the average shear stresses provided by Eq. (1) are useful when evaluating interlaminar shear strength values and comparing creep behavior of specimens subjected to identical mechanical tests in different environments. It is noteworthy that in all tests reported here, the DNS specimens failed in shear mode along the shear plane.

Microstructures of the Hi-N/SiC-B<sub>4</sub>C specimens were characterized by optical microscopy (Zeiss Discovery V12) and SEM (Quanta 450) before and after testing. The specimen subjected to 100 h of creep at 1200°C in steam was also examined using EPMA and WDS to gain insight into the atomic composition at the specimen surface and interior. A JEOL JXA-733 SuperProbe equipped with a WDS attachment was employed for film composition analysis. The specimen was cut parallel to the notch 10 mm away from the shear plane and mounted on carbon tape. Composition of the composite on the fracture surface (i.e. the shear plane) was analyzed. An exposed cross section (surface of the original notch) and a freshly cut cross section were also examined. While energy dispersive spectroscopy is a tool more commonly used to evaluate composite materials systems [35, 36] this study used WDS due to its enhanced accuracy. As no elements with  $Z < 5$  were analyzed the geometric limitation of WDS were not an issue.

### 3. Results and discussion

#### 3.1 Interlaminar shear strength

The interlaminar shear strength (ILSS) was assessed in compression tests to failure performed at 1200°C in air. Typical interlaminar shear stress vs. compressive strain curves shown in Fig. 3 are nearly linear to failure. The average ILSS was 27.2 MPa. Note that Choi et al. [32] obtained similar ILSS values (20–30 MPa) for a 2D woven Hi-Nicalon/SiC composite at 1316°C in air.

#### 3.2 Creep in interlaminar shear

Creep-rupture tests were conducted in compression at 1200°C in air and in steam at shear stress levels ranging from 16 MPa (59% ILSS) to 22 MPa (81% ILSS). Results are summarized in Table 1. Creep strain vs. time curves obtained at 1200°C in air and in steam are shown in Fig. 4. All creep curves obtained at 1200°C in air exhibit primary and secondary creep regimes. Transition from primary to secondary creep occurs fairly early in creep life. Secondary creep persists for the duration of the creep

## Testing and Modeling Ceramic & Carbon Matrix Composites

**Table 1.** Results of creep-rupture tests in interlaminar shear for Hi-Nicalon™/SiC-B<sub>4</sub>C CMC at 1200°C in laboratory air and in steam.

Creep Stress (MPa)	Creep Strain (%)	Time to Rupture (h)
Laboratory Air		
16	0.11	100*
18	0.15	83.0
18	0.14	78.0
20	0.21	26.3
20	0.22	24.1
22	0.08	6.10
22	0.25	17.3
Steam		
16	0.17	100*
18	0.18	73.0
18	0.15	67.0
20	0.20	21.0
20	0.23	18.9
22	0.22	15.9
22	0.25	14.0

\*Run out.

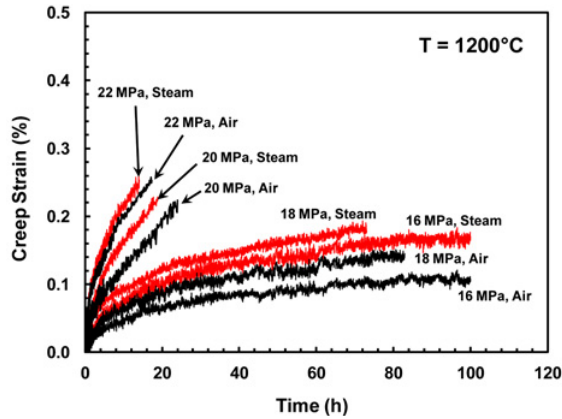


**Figure 4.** Creep strain vs. time curves for Hi-N/SiC-B<sub>4</sub>C CMC obtained at applied interlaminar shear stresses in the 16–22 MPa range at 1200°C in air and in steam.

lifetime. In air, creep run-out of 100h is achieved at the shear stress of 16 MPa (59% ILSS). Creep strains accumulated in air are comparable to the failure strains obtained in compression tests. As was the case at 1200°C in air, all creep vs. time curves obtained in steam exhibit primary and secondary creep, but no tertiary creep regime. Presence of steam has little effect on the creep run-out stress. Creep run-out is achieved at 16MPa both in air and in steam. Creep strains accumulated in steam are also comparable to those produced in air.

Minimum creep rate was measured in all tests. Creep strain rate as a function of applied shear stress is shown in Fig. 5. In air as well as in steam, the minimum creep rate increases by at least an order of magnitude when the applied stress increases from 16 to 22 MPa. The creep strain rates produced in steam can be somewhat higher than those obtained in air. Yet, the overall effect of steam on secondary creep rate does not appear to be dramatic. Stress-rupture behavior is summarized in Fig. 6, where the applied shear stress is plotted vs. time to rupture at 1200°C in air and in steam. Results in Fig. 6 do not reveal significant degradation in creep performance due to steam. The same creep run-out stress is

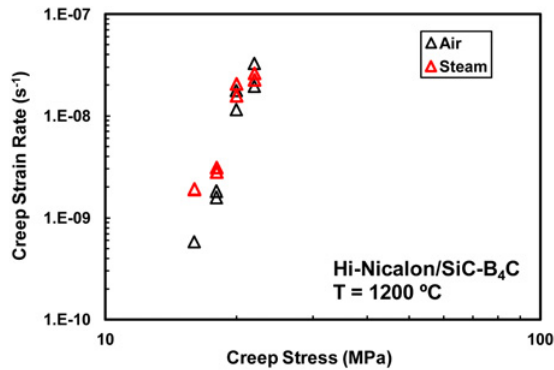


**Figure 5.** Minimum creep rate as a function of applied interlaminar shear stress for Hi-N/SiC-B<sub>4</sub>C CMC at 1200°C in air and in steam.

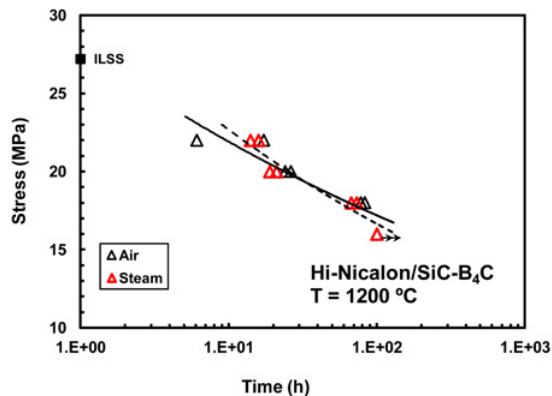


**Figure 6.** Interlaminar shear stress vs. time to rupture for Hi-N/SiC-B<sub>4</sub>C CMC at 1200°C in air and in steam.

produced in air and in steam. At shear stresses above 16 MPa, similar creep lifetimes are produced in steam and in air.

Retained strength and stiffness of the specimens that achieved creep run-out were evaluated in compression tests performed at 1200°C in air. The specimen subjected to 100 h of prior creep in air exhibited virtually no loss of ILSS producing the strength of 26 MPa. Contrastingly, prior creep at 1200°C in steam degraded the ILSS by approximately 25%.

### 3.3 Composite microstructure

When a specimen failed the testing system was promptly shut off and the bottom half of the failed specimen was removed from the furnace. Hence the interior of the fracture surface of the bottom half of the failed specimen was exposed to significant temperatures and prolonged oxidation for a few minutes at most. These are the fracture surfaces that were examined with optical microscopy and the SEM.

Figure 7 shows a typical fracture surface of the DNS specimen tested in compression to failure at 1200°C in air (test duration < 5 s). Fracture occurs along the shear plane primarily through delamination of woven 0/90 fiber layers from the matrix-rich regions, with minimal fiber fracture. The fracture surface shown in Figs. 7a and 7b is largely clean and smooth, indicating that a single fiber layer is associated

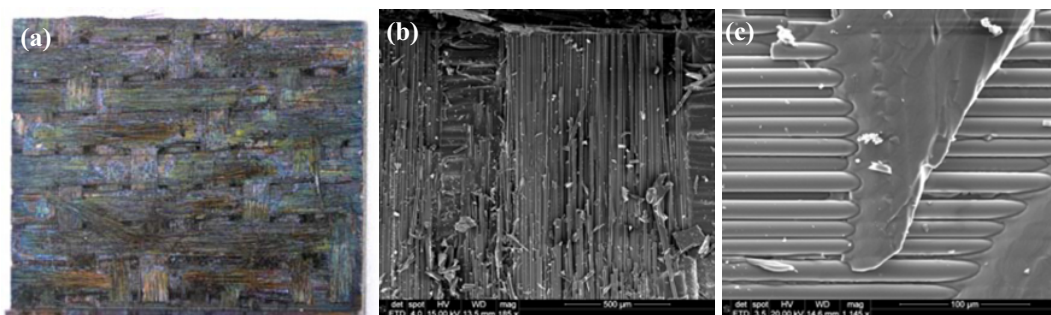


**Figure 7.** Fracture surface of the DNS specimen tested in compression to failure at 1200°C in air. Test duration < 5 s.

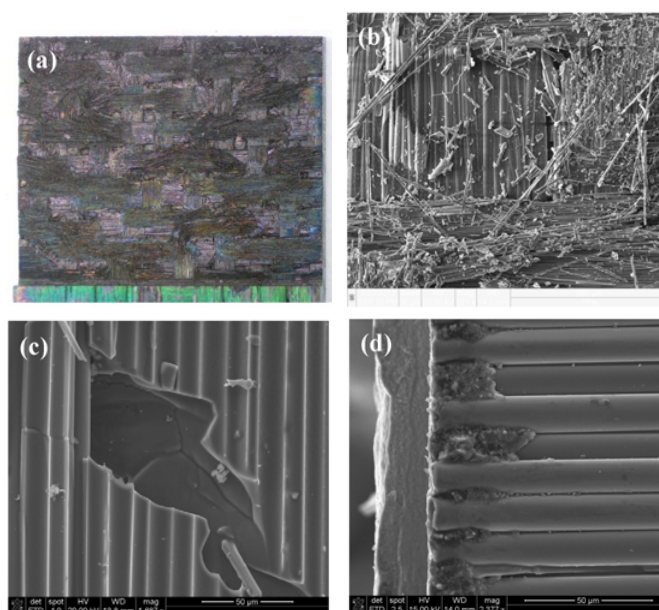


**Figure 8.** Fracture surface of the DNS specimen tested in creep at 20 MPa at 1200°C in air,  $t_f = 26.3$  h.

with delamination. Only small amounts of matrix material remain bonded to the exposed fibers (see higher magnification view in Fig. 7c).

In contrast, the fracture surfaces of the DNS specimens tested in creep at 1200°C in air reveal that the failure mechanism changes with increasing test duration. Consider the fracture surface in Fig. 8 produced in the 20 MPa creep test (test duration is 26.3 h). Fiber fracture and matrix damage are becoming prevalent (Figs. 8a, 8b). Still, a few areas of clean interplay delamination remain. For example see a higher magnification image in Fig. 8c, which shows grooves left in the matrix by the fibers in the course of delamination. Small amounts of glassy phase (believed to be boria) are observed at the periphery of the fracture surface (Fig. 8d).

Figure 9 shows the fracture surface obtained in compression to failure test on a specimen subjected to 100 h of prior creep at 16 MPa in air. Extensive fiber fracture is evident. The fracture surface is dominated by areas exposing multiple 0/90 fiber layers. The failure mechanism has changed from

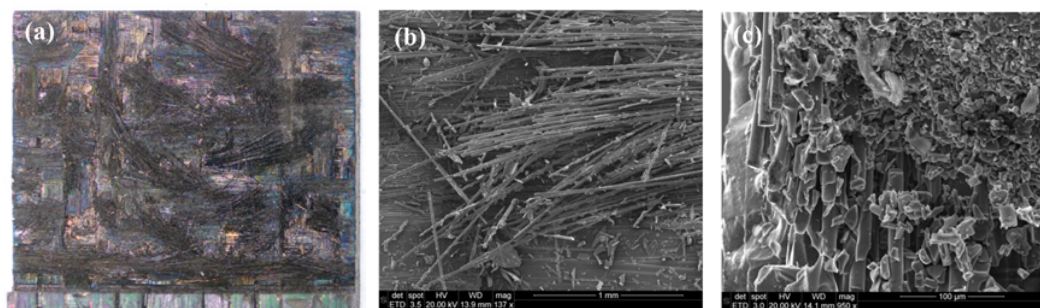


**Figure 9.** Fracture surface of the DNS specimen tested in creep at 16 MPa at 1200°C in air,  $t_f > 100$  h.

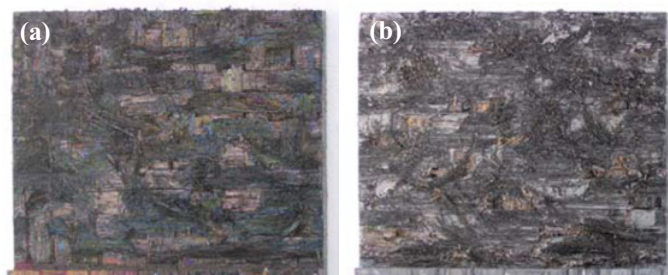


**Figure 10.** Fracture surfaces of the DNS specimens tested in creep at 1200°C in steam: (a) at 20 MPa,  $t_f = 19$  h; (b) at 16 MPa,  $t_f > 100$  h.

interplay delamination to fracture of fiber tows. Yet, even such prolonged exposure at 1200°C in air did not result in significant formation of the glassy phase on the fracture surface. Only minimal amounts of glassy phase are observed at the edges, whereas virtually none are seen in the interior of the fracture surface.

Fracture surfaces produced in steam also show that as the test duration increases the failure mechanism changes from interplay delamination to fiber fracture. Fracture surface obtained in the 20 MPa creep test in steam (Fig. 10a) is also dominated by areas of fiber fracture and matrix damage. The fracture surface obtained after 100 h of creep in steam (Fig. 10b) exhibits massive fiber fracture. No areas of clean interplay delamination can be found. Areas of violent failure exposing multiple fiber layers are seen throughout the fracture surface (Fig. 11a). Extensive fiber-matrix bonding is also observed (Fig. 11b). Furthermore, a much greater amount of the glassy phase is seen on fracture surfaces produced in steam compared to those obtained in air. The key feature of all fracture surfaces produced in steam is the widespread formation of the glassy phase. A large amount of glassy phase is observed at the periphery of the fracture surface (Fig. 11c). Furthermore it appears that the glassy phase located at the edges of the fracture surface (Fig. 11c) has crystallized and cracks have developed after cooling down to room temperature. While a substantial amount of glassy phase is deposited at the edges of the fracture surface, a significant amount is also seen covering the interior of the fracture surface (Fig. 11d).

The Hi-N/SiC-B<sub>4</sub>C composite contains a layered SiC-based matrix, which includes concentric layers of the crack arresting B<sub>4</sub>C around groups of fibers. At 1200°C in air or in steam, SiC and B<sub>4</sub>C oxidize producing fluid glassy phases, which can fill the matrix cracks as soon as they are formed, thus inhibiting the diffusion of oxygen along crack paths and improving the oxidation resistance of the composite. Matrix cracks develop when the load is applied. During loading of the DNS specimens in compression, glass formed within the matrix cracks is largely squeezed out of the cracks towards the edges of the

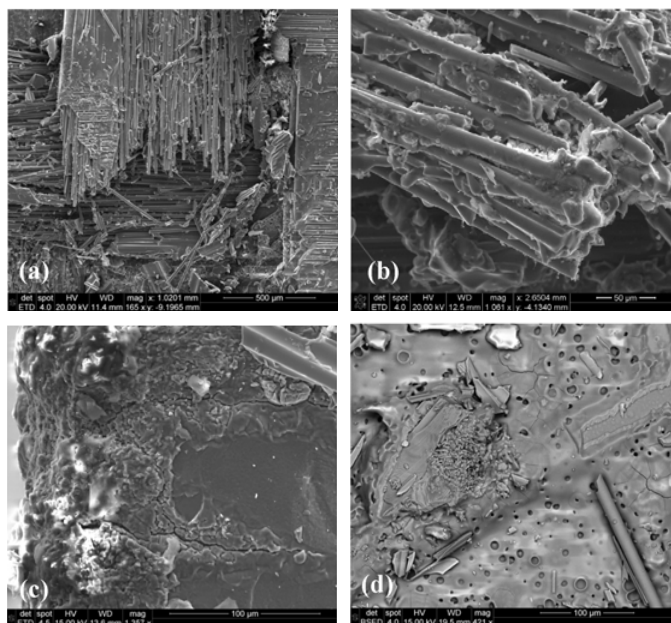


**Figure 11.** Fracture surface of the DNS specimen tested in creep at 16 MPa at 1200°C in steam,  $t_f > 100$  h.

specimen. The amount of glassy phase produced in air appears to be sufficient to form deposits at the edges of the fracture surfaces, but not to cover the interior of the fracture surface as well. Conversely, much larger amounts of the glassy phase are produced in steam as evidenced by considerable glass deposits at the periphery as well as in the interior of the fracture surfaces.

It is likely that in steam the oxidation of the  $B_4C$  layers and formation of boria glass is followed by the oxidation of the SiC matrix layers, thus resulting in the formation of the borosilicate glass during the test. Bubbles seen in the glassy layer covering the fracture surface obtained in the 20 MPa creep test in steam (Fig. 12a) are most likely the gaseous reaction products diffusing through the borosilicate glass. Recall that the borosilicate glass has a higher viscosity than boria, thereby making it more difficult for the gaseous reaction products to escape. The WDS results presented below show that the composition of the glassy layer covering the fracture surface changes to  $SiO_2$  as the test duration in steam increases to exceed 100 h. At 1200°C in steam, the viscosity of the  $SiO_2$  layer decreases [37], allowing the gaseous reaction products to escape. Note the “craters” in the fracture surface obtained after 100 h of creep in steam (Fig. 12b), which are left in the  $SiO_2$  glassy layer by escaping gases believed to be boron-containing complexes.

### 3.4 Wavelength dispersive spectroscopy (WDS)

A WDS analysis of the specimen subjected to 100 h of creep at 1200°C in steam was performed to gain insight into the atomic composition at the specimen surface and interior. The specimen fracture surface (the shear plane parallel to the specimen axis), the exposed cross-section (surface of the notch normal to the specimen axis) and the unexposed cross-section (freshly cut section normal to the specimen axis) were analyzed.

Figure 13 shows an SEM micrograph of the specimen cross-section that was not directly exposed to steam environment. Four areas (A, B, C, D) of the cross-section in Fig. 13 were analyzed with WDS. The analysis of a Hi-Nicalon SiC fiber in the interior of the cross-section (sample A) shows the expected

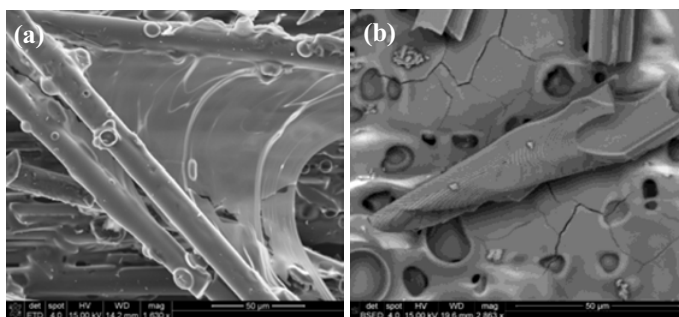
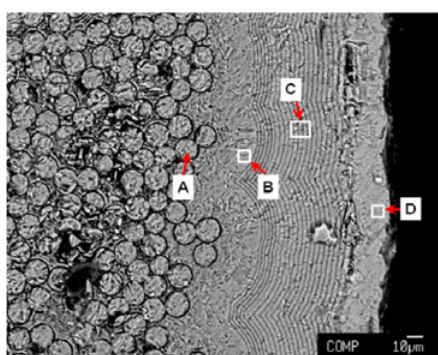


**Figure 12.** Glassy phase covering the interior of the fracture surfaces obtained at 1200°C in steam. (a) Creep at 20 MPa,  $t_f = 19$  h. (b) Creep at 16 MPa,  $t_f > 100$  h.



Sample	B	O	Si	C
A	0	2.0	48.2	49.8
B	43.4	1.1	31.2	24.3
C	18.4	0.7	42.7	38.2
D	3.3	61.8	30.9	4.0

**Figure 13.** SEM composition image of a freshly cut cross section with areas of WDS sampling labeled. Sample A shows a near stoichiometry of a SiC Hi-Nicalon fiber in the cross-section interior. Samples B and C reveal a decrease in B concentration as the exposed surface is approached. Sample D shows formation of a SiO<sub>2</sub> layer on the exposed surface.

nearly one to one ratio of silicon to carbon with minor oxidation. Analysis of the multilayered matrix (samples B and C) reveals a decrease in boron concentration as the exposed surface is approached. The exposed surface (sample D) on the periphery of the cross-section exhibits significant oxidation resulting in formation of an oxidized layer of about 20- $\mu$ m thickness. The WDS analysis of the oxidized layer (sample D) shows a nearly two to one ratio of oxygen to silicon as would be expected for SiO<sub>2</sub>. Only trace amounts of carbon and boron are found in the oxidized layer. SEM micrographs of the exposed cross-section (surface of the original notch) are shown in Fig. 14. As expected, the exposed cross-section is completely oxidized. Elemental analysis in Fig. 14a reveals the composition of the oxidized layer – 66.7% oxygen, 32.4% silicon and traces (<0.5%) of boron or carbon. Figure 14b shows a region of the exposed cross-section where SiC fibers are also visible. The WDS analysis of fiber surface shows 13.3% oxygen, 46.2% silicon and 39.2% carbon. Notably the WDS analysis of other fiber surfaces in Fig. 14b revealed a similar trend with carbon concentration being lower than that of the silicon.

A typical compositional SEM image of the fracture surface (i.e. shear plane) is presented in Fig. 15. While oxidation of exposed surfaces is expected, it is necessary to determine whether similar oxidation process has occurred on the fracture surface and whether any unique reaction products were created. Multiple WDS samplings show that boron concentration remains consistently below 5% across the shear fracture surface, making formation of boron surface complexes highly unlikely. As seen in Fig. 15, some regions of the fracture surface show numerous “craters”. Elemental composition of such a region

## Testing and Modeling Ceramic & Carbon Matrix Composites

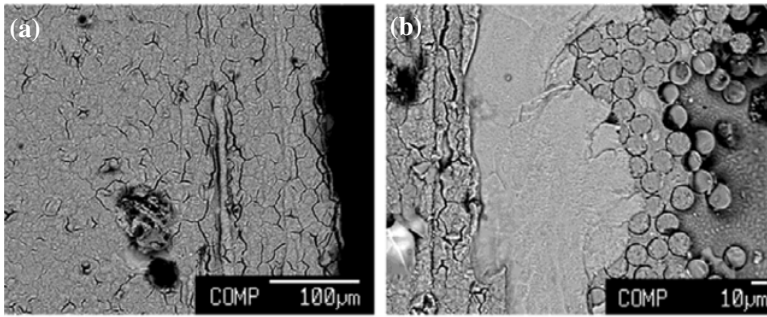
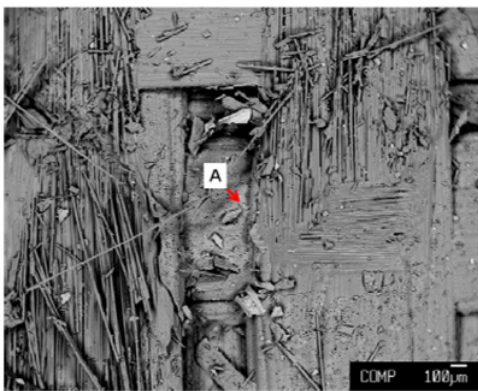


**Figure 14.** (a) SEM composition image of exposed notch showing complete oxidation with a clear loss of features seen in Fig. 13. (b) A region on the notch with exposed fibers also showing oxidation.



Sample	B	O	Si	C
A	2.8	68.5	28.7	0.0

**Figure 15.** (a) SEM composition image of the fracture surface (shear plane) with area of WDS sampling labeled.

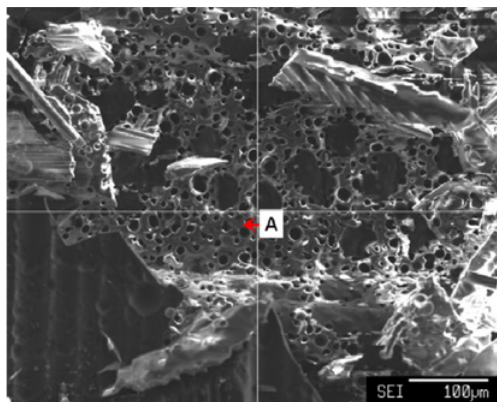


**Figure 16.** Secondary electron image of the fracture surface (shear plane) with area of WDS sampling labeled.

(sample A in Fig. 15) is closely related to SiO<sub>2</sub> and shows no detectable carbon. To more gain better understanding of the composition of the regions containing craters we turn to a secondary electron image of the fracture surface (Fig. 16). WDS analysis of a region exhibiting multiple craters (sample A in Fig. 16) yields a composition of 61.1% oxygen and 33.1% silicon with less than 1% carbon, suggesting formation a glassy SiO<sub>2</sub> layer. After 100 h under load in steam, the viscosity of the glassy SiO<sub>2</sub> layer is expected to decrease [37], allowing the gaseous reaction products to escape and leave craters behind.

#### 4. Concluding remarks

Creep behavior in interlaminar shear of the Hi-Nicalon™/SiC-B<sub>4</sub>C composite was studied at 1200°C in laboratory air and in steam using DNS test specimens. The average ILSS was 27.2 MPa. At 1200°C in air as well as in steam, the Hi-Nicalon™/SiC-B<sub>4</sub>C composite exhibits primary and secondary creep regimes, but no tertiary creep. Creep strains accumulated in steam are only slightly higher than those produced in air. Creep strain rates range from  $5.8 \times 10^{-10} \text{ s}^{-1}$  to  $2.3 \times 10^{-8} \text{ s}^{-1}$  and are little influenced by the presence of steam. Moreover, steam only moderately affects creep lifetimes. The 100-h creep run-out was achieved at 16 MPa in both air and steam. Prior creep at 1200°C in air had little effect on the ILSS. Conversely, prior creep in steam reduced the ILSS by approximately 25%.

At 1200°C in air and in steam, the dominant failure mechanism changes with increasing test duration. In tests of shorter duration failure occurs primarily through interplay delamination with minimal fiber fracture. Generally, only one 0/90 woven fiber layer is associated with delamination. In tests of longer duration (> 30 h) fiber fracture becomes the prevailing failure mechanism. Glassy phase is seen in all fracture surfaces. Much larger amounts of glassy phase are produced in steam than in air. Only minimal amounts of the glassy phase, believed to be borica, are found at the periphery of the fracture surfaces obtained in air. In contrast, copious amounts of glassy phase are found both at the periphery and in the interior of the fracture surfaces obtained in steam. Amount of glassy phase produced in steam increases with test duration. It is believed that in steam, the oxidation of the B<sub>4</sub>C layers and formation of the borica glass is followed by oxidation of the SiC layers in the multilayered self-healing matrix, resulting in the formation of the borosilicate glass. The elemental analysis shows strong evidence of near full oxidation with decreasing concentrations of boron and carbon on exposed surfaces as well as on the fracture surface.

#### References

- [1] D. Brewer, *Mat. Sci. Eng. A*, **A261**, pp. 284–91 (1999)
- [2] D. Brewer, G. Ojard, M. Gibler, *ASME Turbo Expo 2000*, ASME Paper 2000-GT-0670 (2000)
- [3] G.S. Corman, K. Luthra, In: N. Bansal, editor. *Hand book of ceramic composites*, NY: Kluwer Academic, pp. 99–115 (2005)
- [4] G.N. Morscher, G. Ojard, R. Miller, Y. Gowayed, U. Santhosh, J. Ahmad, R. John, *Comp. Sci. Technol.*, **68**, pp. 3305–13 (2008)
- [5] J.C. McNulty, M.Y. He, F.W. Zok, *Comp. Sci. Technol.*, **61**, pp. 1331–38 (2001)
- [6] K.M. Prewo, J.A. Batt, *J. Mat. Sci.*, **23**, pp. 523–527 (1988)
- [7] Mah, T., Hecht, N.L., McCullum, D.E., Hoenigman, J.R., Kim, H.M., Katz, A.P., Lipsitt, H.A., 1984, “Thermal stability of SiC fibres (Nicalon),” *J. Mat. Sci.*, **19**, pp.1191–1201
- [8] F.E. Heredia, J.C. McNulty, F.W. Zok, A.G. Evans, *J. Am. Ceram. Soc.*, **78**, pp. 2097–100 (1995)
- [9] K.L. More, P.F. Tortorelli, M.K. Ferber, J.R. Keiser, *J. Am. Ceram. Soc.*, **83**(1), pp. 211–213 (2000)
- [10] R. Naslain, *Comp. Sci. Technol.*, **64**, pp. 155–170 (2004)
- [11] R. Naslain, R. Pailler, J. Lamon, *J. Eur. Ceram. Soc.*, **7**(3), pp. 263–75 (2010)
- [12] R. Naslain, *J. Eur. Ceram. Soc.*, **2**(2), pp. 75–84 (2005)

- [13] F. Lamouroux, S. Bertrand, R. Pailler, R. Naslain, M. Cataldi, *Comp. Sci. Technol.*, **59**, pp. 1073–85 (1999)
- [14] F. Lamouroux, S. Bertrand, R. Pailler, R. Naslain, *Key Eng. Mater.*, **164–165**, pp. 365–8 (1999)
- [15] S. Darzens, G. Farizy, J. Vicens, J.L. Chermant, In: W. Krenkel et al., editors. *High temperature ceramic matrix composites*. Weinheim (Germany): Wiley-VCH; pp. 211–7 (2001)
- [16] L. Quemard, F. Rebillat, A. Guette, H. Tawil, C. Louchet-Pouillier, C., *J. Eur. Ceram. Soc.*, **27**, pp. 2085–2094 (2007)
- [17] S. Zhu, M. Mizuno, Y. Kagawa, J. Cao, Y. Nagano, H. Kaya, *J. Am. Ceram. Soc.*, **82**(1), pp. 117–28 (1999)
- [18] S. Zhu, M. Mizuno, Y. Kagawa, Y. Mutoh, *Comp. Sci. Technol.*, **59**, pp. 833–51 (1999)
- [19] J. Chermant, G. Boitier, S. Darzens, G. Farizy, J.C. Vicens, J. Sangleboeuf, *J. Eur. Ceram. Soc.*, **22**, pp. 2443–60 (2002)
- [20] M.B. Ruggles-Wrenn, D.T. Christensen, A.L. Chamberlain, J.E. Lane, T.S. Cook, *Comp. Sci. Technol.*, **71**(2), pp. 190–196 (2011)
- [21] P. Carrere and J. Lamon, *Key Eng. Mater.*, **164-165**, pp. 321–4 (1999)
- [22] P. Reynaud, D. Rouby, G. Fantozzi, *Ann. Chim. Sci. Mat.*, **30**(6), pp. 649–58 (2005)
- [23] S. Darzens, J.L. Chermant, J. Vicens, J.C. Sangleboeuf, *Mat.*, **47**, pp. 433–439 (2002)
- [24] P. Carrere and J. Lamon, *J. Eur. Ceram. Soc.*, **23**, pp. 1105–14 (2003)
- [25] M.B. Ruggles-Wrenn, J. Delapasse, A.L. Chamberlain, J.E. Lane, T.S. Cook, *Mat. Sci. Eng. A*, **534**, pp. 119–128 (2012)
- [26] M.B. Ruggles-Wrenn and T.P. Jones, *Int. J. Fatigue*, **47**, pp. 154–160 (2013)
- [27] M.B. Ruggles-Wrenn and G. Kurtz, *App. Compos. Mat.*, **20**, pp. 891–905 (2013)
- [28] S.R. Choi, R.W. Kowalik, D.J. Alexander, N.P. Bansal, *Ceram. Eng. Sci. Proc.*, **28**(2), pp. 179–189 (2007)
- [29] S.R. Choi and N.P. Bansal, *Ceram. Trans.*, **175**, pp. 119–134 (2006)
- [30] S.R. Choi and N.P. Bansal, *J. Am. Ceram. Soc.*, **87**(10), pp. 912–918 (2004)
- [31] S.R. Choi, N.P. Bansal, A.M. Calomino, M.J. Verrilli, *Ceram Trans*, **165**, pp. 131–145 (2005)
- [32] S.R. Choi, R.W. Kowalik, D.J. Alexander, N.P. Bansal, *Comp. Sci. Technol.*, **59**, pp. 890–897 (2009)
- [33] M.B. Ruggles-Wrenn and P.D. Laffey, *Comp. Sci. Technol.*, **68**(10-11), pp. 2260–2266 (2008)
- [34] ASTM C 1425, **15.01**. West Conshohocken PA, Annual book of ASTM Standards (2006)
- [35] I.D. Choi, D.K. Matlock and D.L. Olson, *J Metallurg Trans A*, **21**(9), pp. 2513–2520 (1990)
- [36] J.-M. Yang, S.M. Jeng, K. Bain, and R.A. Amato, *Acta Mat*, **45**(1), pp. 295–308 (1997)
- [37] N.M. Parikh, *J. Am. Ceram. Soc.*, **41**(1), pp. 18–22 (1958)